

# DART-PIM: DNA read mApping acceleRaTor Using Processing-In-Memory

Rotem Ben-Hur, Orian Leitersdorf, Ronny Ronen, , Lidor Goldshmidt, Idan Magram, Lior Kaplum, Leonid Yavitz, and Shahar Kvatinsky,

**Abstract**—Genome analysis has revolutionized fields such as personalized medicine and forensics. Modern sequencing machines generate vast amounts of fragmented strings of genome data called *reads*. The alignment of these reads into a complete DNA sequence of an organism (the *read mapping* process) requires extensive data transfer between processing units and memory, leading to execution bottlenecks. Prior studies have primarily focused on accelerating specific stages of the read-mapping task. Conversely, this paper introduces a holistic framework called DART-PIM that accelerates the entire read-mapping process. DART-PIM facilitates digital processing-in-memory (PIM) for an end-to-end acceleration of the entire read-mapping process, from indexing using a unique data organization schema to filtering and read alignment with an optimized Wagner-Fischer algorithm. A comprehensive performance evaluation with real genomic data shows that DART-PIM achieves a  $5.7\times$  and  $257\times$  improvement in throughput and a  $92\times$  and  $27\times$  energy efficiency enhancement compared to state-of-the-art GPU and PIM implementations, respectively.

## I. INTRODUCTION

Genome analysis serves as the cornerstone of numerous scientific and medical breakthroughs, playing a vital role in personalized medicine [11], [23], [33], [41] and advanced forensics [18], [116]. Genome sequencing machines [50]–[52], [86] produce vast volumes of short random fragmented strings of bases (A, C, G, T in DNA), commonly referred to as *reads*, which are extracted from the longer original DNA [4]. The process of reconstructing the original DNA sequence begins by approximating the location of each read in the overall genome and then using the reads at each location to deduce the most likely reference base. This procedure involves complex algorithms with high memory requirements that constitute a bottleneck to the entire genome analysis process.

*Sequence alignment* is a popular approach that localizes read fragments based on their similarity to a corresponding *reference genome* of the target species. This approach is feasible thanks to the high degree (above 99%) of resemblance between genomes of different specimens within the same species. This computational process, called *read mapping* [4], [21], involves offline *indexing* of the reference genome (utilizing short representative fragments known as minimizers [93]), followed by three consecutive online steps (illustrated in Figure 1): (1) *Seeding* of potential locations (PLs) in the reference genome based on read and reference minimizer similarity; (2) *pre-alignment filtering* to eliminate false PLs; and (3) *read alignment* that determines the most probable PL according to a similarity metric. This latter stage is the most computationally

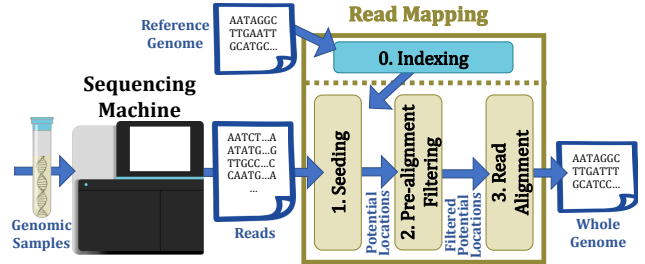


Fig. 1. Genome sequence alignment process. The genomic samples are input into a sequencing machine that fragments them into small segments. The sequencing machine generates short strings known as **reads**, which are then processed during the **read-mapping** procedure. Read mapping involves an offline indexing stage followed by the online seeding, pre-alignment filtering, and read alignment stages.

intensive task, invoking string matching algorithms [40], [80], [105] for each read and PL within the complete genome.

State-of-the-art read alignment techniques predominantly employ a dynamic programming (DP)-based approach, such as the Needleman-Wunsch or Smith-Waterman algorithms [68], [81], [97]. The complexity of these algorithms follows quadratic scaling in execution time and memory usage, thereby generating a significant latency and energy bottleneck [4], [6], [48], [79], [104]. This read-mapping bottleneck has been exacerbated by the recent enhancements of read generation rates on the one hand and insufficient corresponding growth in computational power on the other [4], [42].

To bridge the gap between read volumes and compute capabilities, prior work focused mainly on accelerating each read-mapping stage separately. This effort often prioritizes optimizing read alignment due to its significant computational demands, which can consume over 70% of the read-mapping execution time [19], [20], [26], [36], [60], [61], [79]. Read mapping, however, involves not only the processing of huge datasets, but also the frequent movements of huge volumes of data between the processor(s) and memory units, which increase both execution time and energy consumption [4], [77]. Since the data being transferred throughout the read-mapping process is roughly  $100\times$  larger than the original input reads, the acceleration of computational tasks across the process is still bottlenecked by the data transfer between the processes.

Numerous studies have proposed alternative approaches to efficiently process large amounts of reads [19], [20], [26], [36], [60], [61], [79]. For instance, the state-of-the-art read mapper SeGraM [20] leverages near-memory computing [91] within

a 3D-stacked memory architecture to mitigate costly chip-to-chip data transfers. Consequently, SeGram’s read alignment process alone achieves a  $144\times$  speedup over existing CPU-executed software read mappers, alongside a  $4.4\times$  power consumption reduction. Nevertheless, when handling the entire read-mapping process, SeGram’s performance demonstrates only a  $2.5\times$  speedup for short reads over the existing CPU-based read mappers.

A promising solution to overcoming the data transfer bottleneck involves conducting read-mapping computations directly within the memory. This approach utilizes digital processing-in-memory (*PIM*) techniques to enable high parallelism, eliminating the need for frequent data transfer between the memory and the processor [78]. This paper presents *DART-PIM*, a DNA read mApping acceleRaTor using Processing-In-Memory, which is a comprehensive framework for accelerating the entire read-mapping process. The uniqueness of *DART-PIM* lies in its ability to execute all read-mapping stages for a given read and PL inside a single memory crossbar array. The majority of computations are performed using the memory cells, thus circumventing the data transfer bottleneck. A small number of complementary operations are executed in adjacent RISC-V cores. A key element for efficient computation in *DART-PIM* is careful organization of the reads and the reference genome within memory instances to minimize data transfer along all steps of read mapping. Within these instances, the data allocation is optimized for maximal utilization of the inherent massive parallelism offered by *PIM*. Consequently, *DART-PIM* greatly enhances the performance and energy efficiency of the entire end-to-end read-mapping process. This paper makes the following main contributions:

- 1) We propose a novel end-to-end accelerator architecture for the entire read-mapping process.
- 2) We present a data organization technique for accelerated indexing and seeding of a reference genome.
- 3) We develop a high-performance, memory efficient, in-memory pre-alignment filtering mechanism based on the linear Wagner-Fischer algorithm [107].
- 4) We improved read alignment in-memory performance by enhancing the Wagner-Fischer algorithm with an affine-gap penalty and traceback capability.
- 5) We build system-level simulators that use real genome datasets to ensure precise evaluation of *DART-PIM*’s accuracy and performance, and compare it to state-of-the-art implementations (NVIDIA Parbricks [85] and SeGram [20]), demonstrating faster execution time ( $5.7\times$  and  $257\times$  improvement, respectively) and improved energy efficiency ( $92\times$  and  $27\times$ , respectively).

## II. BACKGROUND: READ MAPPING AND ITS LIMITATIONS

The read-mapping process comprises three sequential online stages, preceded by an offline indexing procedure. The classical indexing approach generates a database that matches any sub-string of length  $k$  (typically, 12) appearing in the reference genome (called *k-mer*) with pointers to all locations of this sub-string within the genome [70]. Although lossless,

the practicality of this approach is limited due to its extensive memory demands. A more practical approach indexes the genome to select *minimizers* [93], rather than *k-mers*, which reduces the number of *k-mers* associated with each reference segment while achieving accurate compressed representation.

Once the indexing stage is completed, the database is stored and each new DNA sample can be sequenced by employing the following three steps: (1) seeding, (2) pre-alignment filtering, and (3) read alignment. These steps are performed sequentially for any new read (typically, strings comprising 100 to 2000 bases) entering the system. The purpose of the seeding stage is to identify PLs of the read within the reference genome. The read is processed in sliding windows of length  $W + k - 1$ , where  $W$  is the window size (typically  $W = 30$ ), and each window is represented by its minimizer. The PLs of the read are defined as the set of addresses of all its (unique) minimizers in the reference genome (taken from the indexing database).

Since the sets of PLs are typically large, a filtering procedure is required to reduce the number of PLs per read. Pre-alignment filtering commonly employs heuristic techniques to discard PLs based on dissimilarity between the read and a reference genome segment. For instance, a popular filtering approach, called the base count filter [5], compares histograms of bases for a read and a corresponding segment (eliminating 68% of PLs on average).

The main step of read mapping involves optimal sequence alignment algorithms for read alignment. Since the goal is to determine the most accurate location of each read within the genome, it commonly involves computationally-intensive dynamic-programming algorithms such as the Smith-Waterman (*SW*) algorithm [98] or the Needleman-Wunsch (*NW*) algorithm [82]. While optimal sequence alignment is the obvious candidate for hardware acceleration due to its compute-bound nature, the primary portion of energy and execution time stems from data transfer between the memory and computing cores throughout the sequencing process.

Based on in-house simulations we conducted with a human reference genome (0.8GB in size), seeding generates an average of 1000 (32 bits) PLs per read, which amounts to 1556GB for a typical amount of 389M reads of length 150 (14.6GB in size). Note that while the input data volume to the seeding stage is 14.6GB, it generates approximately a 100 times larger output data volume, which has to be transferred to the memory and back to a pre-alignment filtering accelerator. This data transfer is the system’s primary bottleneck, even with significant acceleration of each individual step. Motivated by this observation, this paper proposes a solution that executes all stages of read mapping within the same memory crossbar array, thereby eliminating the need for data transfers between the different stages.

## III. MODIFIED READ-MAPPING ALGORITHMS USED IN DART-PIM

This section describes the read-mapping algorithms that are employed in *DART-PIM* for efficient processing in-memory. The basic algorithms are the *Linear Wagner-Fischer* and

*Affine Wagner-Fischer* algorithms. The former is used for pre-alignment filtering and the latter for read alignment. The preceding stages of read mapping, i.e., indexing and seeding, only require that the data be carefully arranged within the memory prior to pre-alignment filtering.

State-of-the-art read mappers commonly employ either the Smith-Waterman (SW) algorithm [98] or the Needleman-Wunsch (NW) algorithm [82]. Since the compared strings in DNA sequencing setting are typically similar, these algorithms, which consider sub-string matches, require relatively large bit-width representation (e.g., 8 bits) for storing the similarity score. Hence, supporting read mapping by processing it within the memory may impose a relatively large memory footprint or restrict the sequence length that can be processed efficiently.

To enhance read mapping efficiency, we propose an alternative algorithmic approach that adopts the Wagner-Fischer (WF) algorithm [107], originally used for edit distance computation. We modify the algorithm to output not only the distance metric, but also the traceback (i.e., the aligned sequence itself). Since the WF algorithm counts mismatches, rather than matches, it requires fewer bits (e.g., 3) per distance, thereby being a better fit for processing-in-memory.

We use two variants of the WF algorithm. The first variant, used for pre-alignment filtering, is an adaptation of the classical WF algorithm. We call this the *Linear* WF algorithm. The second variant, used for read alignment, extends the linear WF by enhancing the WF algorithm by (1) accounting for the affine-gap penalty of the SW and NW algorithms, and (2) enabling traceback to reconstruct the aligned sequence. We refer to this as the *Affine* WF algorithm. The affine-gap penalty combines constant and linear gap penalties and is commonly used in biological applications [25], [34].

#### A. Linear Wagner-Fischer Algorithm

Given two input strings  $S_1$  and  $S_2$  (with respective lengths  $n$  and  $m$ ), the linear WF algorithm constructs the *WF distance matrix*,  $D$ , according to the conditions of the WF algorithm, with a size of  $(n + 1) \times (m + 1)$ :

- 1) Initialize the first row and first column as follows:

$$D_{i,0} = \sum_{k=1}^i w_{del}, \text{ for } 1 \leq i \leq n, \quad (1)$$

$$D_{0,j} = \sum_{k=1}^j w_{ins}, \text{ for } 1 \leq j \leq m.$$

- 2) Fill the matrix  $D$ : If  $S_1(i) = S_2(j)$ , then  $D_{i,j} = D_{i-1,j-1}$ ; otherwise,

$$D_{i,j} = \min \left\{ \begin{array}{l} D_{i-1,j} + w_{del}, \\ D_{i,j-1} + w_{ins}, \\ D_{i-1,j-1} + w_{sub} \end{array} \right\}. \quad (2)$$

where  $w_{del}$ ,  $w_{ins}$ , and  $w_{sub}$  are the costs of a deletion, an insertion, and a substitution, respectively. The cost values, as well as additional WF parameters, appear in Table III.

#### B. Modified Affine Wagner-Fischer Algorithm

The affine WF algorithm enhances mapping accuracy (at the cost of complexity) by using a penalty that is represented

as  $w_{op} + w_{ex}(L - 1)$ , where  $w_{op}$  denotes the cost of opening a gap,  $w_{ex}$  represents the cost of extending an existing gap while  $L$  corresponds to the gap length. Since this distance measure achieves higher accuracy at the cost of higher complexity (larger execution time and memory storage), we perform the linear WF algorithm for each PL for pre-alignment filtering, and employ the affine WF only for selected locations based on their linear WF distance. The explicit affine-gap WF matrix is given by

$$D_{i,j} = \begin{cases} D_{i-1,j-1}, & S_1(i) = S_2(j) \\ \min \left\{ \begin{array}{l} M1_{i,j}, \\ M2_{i,j}, \\ D_{i-1,j-1} + w_{sub} \end{array} \right\}, & \begin{array}{l} (\text{ins}) \\ (\text{del}) \\ (\text{sub}) \end{array} \end{cases}, \quad (3)$$

where

$$M1_{i,j} = \min \left\{ \begin{array}{l} M1_{i-1,j} + w_{ex}, \\ D_{i-1,j} + w_{op} + w_{ex} \end{array} \right\}, \quad \begin{array}{l} (\text{extend } S1 \text{ gap}) \\ (\text{open } S1 \text{ gap}) \end{array} \quad (4)$$

and

$$M2_{i,j} = \min \left\{ \begin{array}{l} M2_{i,j-1} + w_{ex}, \\ D_{i,j-1} + w_{op} + w_{ex} \end{array} \right\}, \quad \begin{array}{l} (\text{extend } S2 \text{ gap}) \\ (\text{open } S2 \text{ gap}) \end{array} \quad (5)$$

Due to the iterative nature of the WF algorithms, the  $(i, j)$ -th matrix value  $D_{i,j}$  originates from one of three possible preceding cells (see Eq. 3), the  $(i, j)$ -th matrix values  $M1_{i,j}$ ,  $M2_{i,j}$  originate from one of two possible preceding cells (see Eq. 4 and 5). The affine WF saves the “directions” of the predecessors (4-bit representation) for each matrix cell. The optimal sequence alignment can, therefore, be inferred without having to save the entire matrix for traceback calculation.

## IV. IN-MEMORY EXECUTION OF READ-MAPPING ALGORITHMS

The read mapping execution in DART-PIM leverages digital processing-in-memory (PIM) technologies. Emerging digital PIM architectures (such as DRAM PIM [32], [39], [72], [95], memristive PIM [17], [37], [64], [92], [101], [103] and SRAM PIM [27], [30]) enable massive parallel bitwise operations within memory by integrating logic circuits into the same physical devices used for memory. For explanation and evaluation, we chose to employ bulk bitwise PIM [89], [90], using memristive memory technologies [3], [46], [110]. However, other digital PIM technologies can also be used. This section outlines the basic principles of our approach using the MAGIC NOR gate [64], and explains how a WF iteration is implemented within a single memory crossbar row.

#### A. Memristive Processing-In-Memory

Memristive memories can be used as nonvolatile memories, where each cell within the memory crossbar array consists of a single memristive device whose resistance encodes its logical state. When writing or reading data, appropriate voltages are applied across the desired wordlines and bitlines to modify/sense the resistance of the target memristive devices [113]. These memories can perform computations using the memory cells themselves [16], [38], [44], [64], [88]. Although the

	BL <sub>1</sub>	...	BL <sub>2</sub>	...	BL <sub>2eth+1</sub>
WL <sub>1</sub>	I <sub>1</sub>	J <sub>1</sub>	f{I <sub>1</sub> , J <sub>1</sub> } - Computation result	Intermediate computations	
WL <sub>2</sub>	I <sub>2</sub>	J <sub>2</sub>	f{I <sub>2</sub> , J <sub>2</sub> } - Computation result	Intermediate computations	
⋮	⋮	⋮	⋮	⋮	⋮
WL <sub>n</sub>	I <sub>n</sub>	J <sub>n</sub>	f{I <sub>n</sub> , J <sub>n</sub> } - Computation result	Intermediate computations	

Fig. 2. Area allocation within a memory crossbar array: each row conducts a series of logical operations, starting from  $L$ -bits inputs  $I_x$  (blue) and  $J_x$  (yellow), using intermediate results (orange), to obtain the final output stored in the memory (green). All  $n$  rows perform the same logical operations (over different inputs) concurrently.  $WL_x$  and  $BL_x$  are, respectively, wordline (row) and bitline (column) number  $x$ .

TABLE I  
SUMMARY OF EXECUTION CYCLES FOR MAGIC-NOR-BASED OPERATIONS WITH  $N$ -BIT OPERANDS (UNLESS SPECIFIED OTHERWISE).

Logical Operation	# Cycles
AND	$3N$
XNOR	$4N$
XOR	$5N$
Copy	$1 + N$
Addition of two $N$ -bit in-memory numbers	$9N$
Addition of an $N$ -bit and a single-bit in-memory numbers	$5N$
Addition of one in-memory number and a constant	$5N$
Subtraction of two in-memory numbers	$9N$
Mux between two in-memory numbers	$3N + 1$
Minimum of two in-memory numbers	$12N + 1$

reliability of memristive logic is still challenging, specific strategies have been developed [66], [67], [94] to substantially improve their correct execution and lifetime.

One notable technique for conducting logic operations within an RRAM [3], [109], [113] memristive array is the MAGIC NOR method [64]. This method involves applying voltages to two input memory cells and one output cell in the same row. The output memory cell changes its state according to the NOR function applied to the logical states of the two inputs. The structure of MAGIC NOR allows parallel execution of multiple gates, each in a different row, as long as their columns are aligned. Tools such as [13], [14] can determine the latency-optimal sequence of such operations to accomplish a desired computation. This sequence is implemented using cells within the same row, operating sequentially. When all available cells become occupied by the outputs, the unused cells are initialized and reused for the remaining computations. An illustration of this procedure is depicted in Figure 2.

Implementing read mapping using PIM requires various logical operations. These operations and their corresponding optimized number of clock cycles are listed in Table I.

### B. Wagner-Fischer Algorithm in a Single Crossbar Row

Maximizing the parallelism of bulk-bitwise PIM is crucial in DART-PIM. Full potential is achieved when an entire WF algorithm is executed within a single crossbar row. In this configuration, each row processes a separate instance of the WF algorithm, with different subsets of columns dedicated to specific algorithmic steps. This setup allows simultaneous operations on multiple reads/PLs across the crossbar's columns.

To meet the single-row requirement, we truncate the maximal allowed WF matrix values to  $eth$ , beyond which the

strings are considered too different and the value is saturated. The selection of  $eth$  trades off alignment accuracy for complexity reduction, as it allows to compute in each row only  $2eth+1$  unsaturated cells around the diagonal [106]. We assign 3-bits per value for linear WF (5-bit for affine WF), setting  $eth$  to 6 (31 for affine WF). This maintains accuracy surpassing even the commonly used  $eth = 5$  for linear SW [50].

Algorithm 1 details the steps to calculate a single WF matrix cell using MAGIC NOR operations within a single memory row. Most row cells store the read ( $S_1$ ) and reference segment ( $S_2$ ), while other cells are used for the computation. WF distances have a designated cell subset (*WF distances buffer*), with remaining cells for intermediate computations. This allocation is shown in Figure 3, and WF matrix cell mapping in Figure 4. This core process is optimized for a minimal number of clock cycles.

**Algorithm 1**  $D_{i,j}$  calculation for the linear WF with MAGIC (# MAGIC operations (ops) for a  $b$  bit cell, derived from Table I).

---

**Input:** String characters  $S_1(i), S_2(j)$  and previous WF values  $D_{i-1,j}, D_{i,j-1}, D_{i-1,j-1}$   
**Output:** Next WF value  $D_{i,j}$

- $X = \min\{D_{i-1,j}, D_{i,j-1}\}, Y = \min(X, D_{i-1,j-1})$   $\triangleright 2 \cdot 13b$  ops (adding two  $b$ -bit numbers)
- $Z = Y + 1$   $\triangleright w_{del} = w_{ins} = w_{sub} = 1$   $\triangleright 5b$  ops (adding  $b$ -bit and single bit numbers)
- Set  $S1 = 7$  if  $Y=7$ , and 0 otherwise  $\triangleright$  MUX1 select, 6 ops (two single-bit ANDs)
- Set  $MUX1 = Y$  if  $S1 = 1$ , and  $Z$  otherwise  $\triangleright 3b + 1$  ops
- Set  $S2 = 1$  if  $S1(i) = S2(j)$ , and 0 otherwise  $\triangleright$  MUX2 select, 11 ops (two XNORs + single AND)
- return** MUX2 value as  $D_{i-1,j-1}$  if  $S2=1$ , and MUX1 otherwise  $\triangleright 3b + 1$  ops  $\triangleright$  Total:  $37b + 19$  ops for a single cell

---

**Algorithm 2** The linear WF matrix calculation with  $2eth + 1$  buffer size.

---

**Input:** Strings  $S_1$  (read of length  $N$ ) and  $S_2$  (reference of length  $M$ )  $\triangleright eth$  parameter set to 6  
**Output:** Linear WF distance between  $S_1$  and  $S_2$

- Initialize to zero an array WFd of size  $2eth + 1$  and 3-bit cells  $\triangleright$  WF distances buffer
- for**  $i = 0$  to  $N - 1$  **do**
- for**  $j = 0$  to  $2eth$  **do**
- Set  $WFd[j]$  to one of the following:
- if**  $(j == 0)$  **then**  $\triangleright$  left edge of WFd  
 $\min\{WFd[j] + \mathbb{1}_{S_2[i] \neq S_1[i+j]}, WFd[j + 1] + 1\}$
- else if**  $(j == 2eth)$   $\triangleright$  right edge of WFd  
 $\min\{WFd[j] + \mathbb{1}_{S_2[i] \neq S_1[i+j]}, WFd[j - 1] + 1\}$
- else**  
 $\min\left\{WFd[j] + \mathbb{1}_{S_2[i] \neq S_1[i+j]}, WFd[j - 1] + 1, WFd[j + 1] + 1\right\}$
- end if**
- $WFd[j] = \min\{WFd[j], eth + 1\}$
- end for**
- end for**
- return**  $WFd[eth]$

---

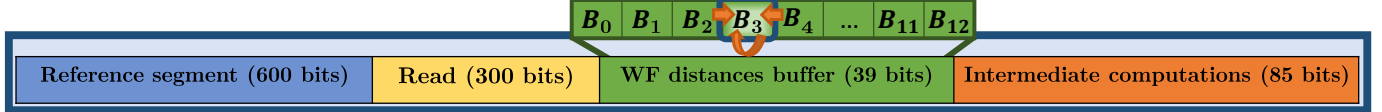


Fig. 3. Mapping of a linear WF matrix calculation into a single crossbar row for  $eth = 6$ . The reference segment (blue) and read (yellow) are the computation inputs. Only  $2eth + 1$  WF distances are needed at any point (green). To compute the current WF distance, only the distances in adjacent cells (storing the top and left WF matrix distances) and the previous value of the current cell (storing the top-left WF matrix distance) are required. The intermediate results generated while computing the distances are stored in temporary row cells (orange), and due to limited number of cells, are re-used when necessary. The total number of bits in the row is 1024.

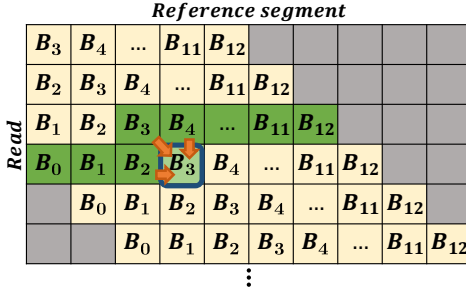


Fig. 4. Example of the mapping of a banded WF matrix (with  $eth = 6$ ) onto the WF distances buffer in a single crossbar row (contained  $2eth + 1$  cells). The computed cell is denoted by light green “ $B_3$ ” (location (4, 4)). The remaining green cells are stored within the WF distances buffer during computation. The computation is performed using only top, top-left, and left cells (marked with orange arrows). Upon completion, the computed value replaces the target cell’s value in the WF distances buffer. Note that gray cells are not computed as they represent distances larger than  $eth$ .

To fit all WF computations in a single row, we minimize crossbar row bits for input data (strings  $S_1$  and  $S_2$ ) and computations. Each WF matrix cell requires only its upper, upper-left, and left neighbors. The cells are computed sequentially within the crossbar row, where only the previous cells required for the present computation are stored at any given time, until the final result in the lower-left cell is reached. For linear WF, the aligned string is not needed, so traceback is not required. The complete WF matrix computation using a buffer of  $2eth + 1$  cells is provided in Algorithm 2.

Similarly, the affine WF computation involves three matrices, each with  $2eth + 1$  cells per row. To reconstruct the aligned string (traceback), we track the edits path by storing the direction of the origin cell for each matrix cell. According to Eq. (3), two bits are needed per cell for the four origin directions. Matrices M1 (Eq. 4) and M2 (Eq. 5), require one bit per cell for their two origin directions. Traceback information is stored in designated rows within the crossbar, occupying 7× more rows than used for computation.

These WF optimizations reduce memory footprint and computational complexity by decreasing the bit-width per WF cell and considering fewer sub/super-diagonals. This lowers the linear WF algorithm latency by 2.8× compared to SW, enabling efficient computation of a full matrix within a single memristive crossbar row (versus two rows in SW).

## V. DART-PIM: DNA READ-MAPPING ACCELERATOR

This section presents the DART-PIM architecture, integrating bulk-bitwise memristive PIM with RISC-V cores. We com-

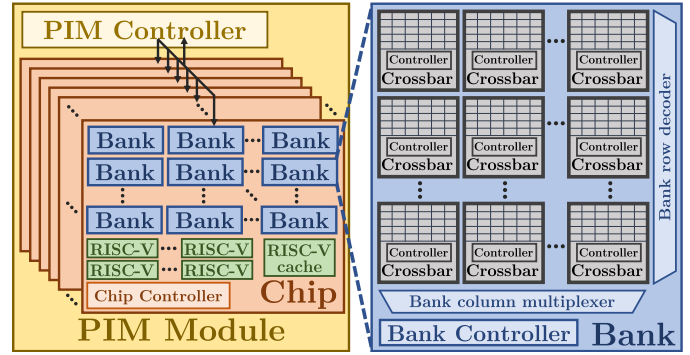


Fig. 5. DART-PIM architecture featuring RISC-V cores and computing memristive memories. The memory consists of a single PIM module, which contains RISC-V cores with private L1 cache memories integrated within the memristive memory chips. Each chip is divided into banks, each equipped with a dedicated controller. Each crossbar in the bank is responsible for a single reference minimizer.

mence by describing DART-PIM’s structure and properties, then explain each stage of read mapping using DART-PIM.

### A. DART-PIM Architecture

The DART-PIM architecture is based on a PIM module, which includes a PIM controller managing multiple memristive chips, similar to standard DRAM main memories [55] (where a PIM module is analogous to a DRAM rank). Each PIM module incorporates several memory chips with two primary components: (1) The DART-PIM memory (*DP-memory*) – A set of banks with a controller and multiple crossbars [55], [101], and (2) the DART-PIM RISC-V (*DP-RISC-V*) – standard RISC-V processors performing a small portion (0.16%) of the affine WF instances, with one processor (the *main RISC-V*) managing data arrangement and high-level processing instructions for all DP-memory cores. The hierarchical structure of DART-PIM is illustrated in Figure 5 with specific architectural parameters given in Table II.

In addition to standard read/write capabilities, the memristive crossbars in DART-PIM support PIM operations with dedicated per-chip controllers. Each chip controller oversees multiple banks and their crossbars. Upon initiating a PIM request, the information is transmitted to the target chip in a write operation format [102]. The designated chip controllers then issue the necessary sequence of MAGIC NOR operations to all associated banks and crossbars. Since all crossbars execute identical tasks, the controllers are quite simple, reducing system area and energy consumption.

TABLE II  
SUMMARY OF DART-PIM ARCHITECTURE CONFIGURATION.

Module property	Value
Total memory capacity	256GB
# PIM Module	1
# Chips per PIM module	32
# Banks per chip	512
# Crossbars per bank	512
# Columns / rows / Bytes per crossbar	1024 / 256 / 32KB
# RISC-V cores per chip	4
Cache capacity per chip	128KB
RISC-V to memory banks BUS width	512 bits

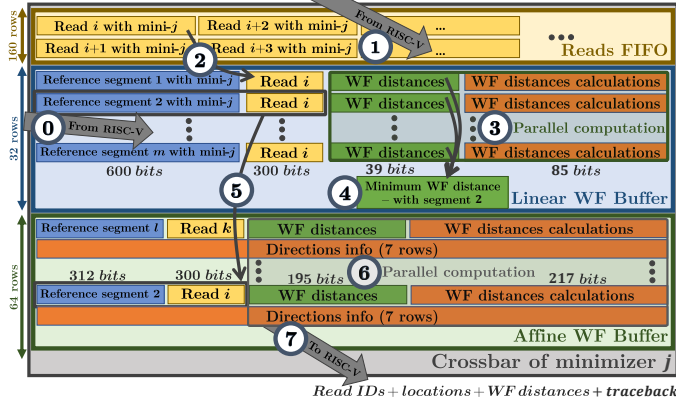


Fig. 6. A memory crossbar with 256 rows and 1024 columns, used for the execution of the WF algorithm between reads and reference segments with minimizer  $j$  ( $mini-j$ ), and  $eth=6$ . The crossbar is divided into three components: (1) Reads FIFO (light yellow), (2) Linear WF Buffer (light blue), and (3) Affine WF Buffer (light green). The numbered circles represent the steps of the entire read-mapping process: (1) indexing – step ①, (1) seeding – step ①, (2) pre-alignment filtering – steps ③ and ④, and (4) read alignment – step ⑥. Steps ② and ⑤ involve intra-crossbar data movements, while step ⑦ entails transmitting the results to the RISC-V. Detailed explanations about this process are given in Sections V-B to V-E.

Each crossbar (or several crossbars, if needed) handles all read-mapping stages of a specific minimizer from the reference genome. DART-PIM supports various read lengths, but the best performance is achieved when a single crossbar row accommodates the entire WF matrix calculation (as splitting a read across multiple rows degrades performance). The row length must, therefore, be at least three times the read size to contain the read (2R bits for R base pairs), the reference (4R bits), and space for intermediate computations/results (minimum  $\sim 80$  bits). To support read lengths up to 150 base pairs [4], each crossbar was allocated 1024 columns by 256 rows [117], partitioned into three subsets corresponding to the three online read-mapping stages: seeding, pre-alignment filtering (via linear WF), and read alignment (via affine WF):

- 1) *Reads FIFO* contains 160 rows  $\times$  three reads per row (total of 480 reads associated with the same minimizer).
- 2) *Linear WF Buffer* contains 32 rows executing multiple instances of the linear WF concurrently for the target minimizer (one instance per row). Each row accommodates a different segment of the reference.
- 3) *Affine WF Buffer* contains 64 rows, where each eight rows facilitate a single affine WF instance (one row

for distance calculations and seven rows for optimal alignment recovery). Thus, eight concurrent execution of the affine WF are supported.

Given a target minimizer, Figure 6 depicts the crossbar layout and execution flow. The numbering refers to the specific tasks performed in each area. Due to high variations in minimizer frequency within the reference genome, different minimizers require different compute resources. Infrequent minimizers induce crossbars with low utilization of the linear WF buffer, thus reducing the effective compute per area efficiency. We, therefore, assign the WF calculation of such minimizers to the DP-RISC-V cores offline, saving significant crossbar area.

Minimizer frequency within reads also varies significantly. Frequent minimizers fill the Reads FIFO, creating a latency bottleneck. To address this, the Reads FIFO is designed to be significantly larger than the compute buffers. As a result, the number of WF matrices computed for the same minimizer is limited, slightly degrading accuracy (shown to be negligible in Section VII-A), while dramatically improving execution time.

### B. Offline Indexing

The offline indexing stage of DART-PIM imports the reference segments themselves (rather than only their addresses) into the linear WF buffers inside the DP-memory crossbars. Each linear WF buffer row is occupied by a single reference segment, representing a single PL, for the minimizer assigned to the relevant crossbar.

The length of the reference segment written to the crossbar is selected to support read alignment regardless of the location of the minimizer within the read. Therefore, the minimum required length is approximately twice the read length, as the minimizer may be at the left/right edge of the read (the precise length is  $2(rl + eth) - k$ , where  $rl$  represents the read length). An illustration of the arrangement of indexing data inside a crossbar is depicted near the ① marker in Figure 6. Figure 7a illustrates how indexing is arranged across different crossbars.

Although this approach duplicates the reference segments across crossbars, it is beneficial as it completely eliminates transfers of reference data throughout the computation. Specifically for the human genome, the storage overhead grows about 17 $\times$ , from 800MB for standard hash-table methods to 13.3GB for DART-PIM. Our results confirm that this strategy is beneficial in terms of latency and energy, saving around 300 billion reference segment transfers from the memory.

### C. Online Seeding

The first online stage of DART-PIM is the seeding of every read to its corresponding reference segments according to the read's set of minimizers. Reads continue to enter the Reads FIFO (① in Figure 6) until one of the crossbars has filled its Reads FIFO. Figure 7b depicts the arrangement of reads across different crossbars according to their minimizers.

The seeding process commences when the main RISC-V core sends a list of reads and their minimizers to the PIM

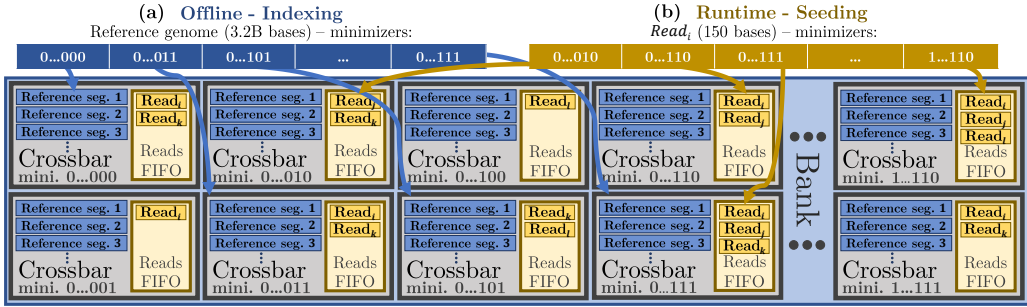


Fig. 7. The crossbars' arrangement of (a) the reference genome during the offline indexing stage, and (b) the reads during the runtime seeding stage.

controllers. Each such controller is aware of all minimizers relevant to any of its descendent controllers in DART-PIM's hierarchy. This way, only relevant reads are propagated throughout DART-PIM to the crossbar controllers, which add them to their Reads FIFO. When one of the Reads FIFO fills up, it signals the PIM controller to stop sending reads; and the same command is sent to the main RISC-V core to stop the read stream and proceed to the pre-alignment filtering stage.

#### D. Online Pre-Alignment Filtering

Pre-alignment filtering in DART-PIM uses the linear WF algorithm. Each read's minimizer is processed by the linear WF to calculate its similarity with all reference segments of its PLs, discarding segments with high distances to reduce the number of PLs per read.

The filtering process begins with the main RISC-V core sending commands to the PIM controller to start WF cell calculations in all DP-memory crossbars. Since the data (read and reference segments) are stored in-memory, the core can send the same instruction to all chip controllers. Each crossbar is then assigned a sequence of MAGIC NOR operations, performing WF matrix cell calculations in its linear WF buffer rows concurrently, as directed by the chip controller—a process we term a *linear WF iteration*.

After each iteration, the processed read is removed from the Reads FIFO. The RISC-V core continues sending reads and repeating the process until all reads are processed and buffers are empty. This stage is computationally intensive and often a bottleneck, making its throughput crucial. Each crossbar sequentially performs the following steps to implement a linear WF iteration, paralleling multiple WF instances:

- 1) First, a read is copied from the Reads FIFO to the crossbar's linear WF buffer (② in Figure 6). At a given linear WF iteration, a crossbar maps a specific minimizer (within a specific read) to multiple reference segments (representing multiple PLs). Hence, the same read is written to all linear WF buffer rows in parallel. Each row performs its computations on a different section of the reference segment, depending on the minimizer's location within the read. This location is given as an address offset to the crossbar controller alongside the read itself.
- 2) The next stage is the *linear WF matrix calculation* (③ in Figure 6). The linear WF matrix is computed within the

linear WF buffer according to instructions generated by the chip controller for all crossbars in parallel. When this stage concludes, each row contains its linear WF distance.

- 3) Consequently, the minimal value is extracted from the distances stored in the different rows of the linear WF buffer (④ in Figure 6). Although computed serially within each crossbar, the minimum extraction is performed in parallel across many crossbars.
- 4) Finally, the selected reference segment, corresponding to the minimal WF distance, is copied alongside the read to an empty row in the affine WF buffer (⑤ in Figure 6). Since the read and the reference segment are already aligned at this stage, it is possible to copy only the required sub-segment, rather than the entire reference segment that was twice as long (see Section V-B).

#### E. Online Read Alignment

As in the linear WF iteration, an *affine WF iteration* starts within a crossbar only when the Affine WF buffer is full. Once invoked, the affine WF iteration (⑥ in Figure 6) is calculated in parallel over all crossbar rows as well as across different crossbars. Recall that an affine WF iteration includes both the WF matrix calculation and traceback recovery.

Finally, the results of the affine WF iteration are sent from each crossbar (specifically, each Affine WF buffer row) to the main RISC-V core (⑦ in Figure 6). The results include the read index, the PL within the reference genome, the affine distance, and the traceback. The RISC-V core maintains in dedicated crossbars a list of reads and their “best so far” PL candidate, obtained by selecting the PL with minimal WF distance received from the DP-memory for every read.

## VI. DART-PIM EVALUATION METHODOLOGY

DART-PIM evaluation consists of assessing its accuracy, execution time, energy, and area. We evaluate the results using several simulators and compare them to the following five state-of-the-art platforms: (1) minimap2 [71], a CPU-based mapper, executed on an Intel® Xeon® E5-2683 v4 CPU [54] with 32 physical cores operating at 2.10GHz, with 256GB DDR4 memory; (2) NVIDIA Parabricks [85], a GPU-based mapper, executed on an NVIDIA DGX A100 (with eight A100 Tensor Core GPUs) [84]; (3) GenASM [19], which accelerates computations within the logic layer of a 3D-stacked memory [1], [49], [56], [65]; (4) SeGram [20], which

improves GenASM throughput at the cost of increased energy and area; and (5) GeNVoM [62], which uses heuristics to improve throughput at the cost of accuracy.

To comprehensively evaluate the DART-PIM architecture, we developed four simulators: (1) a full-system simulator to test the overall behavior and performance; (2) a single-crossbar simulator designed to validate functionality and generate precise metrics for a single WF iteration; (3) a DP-RISC-V simulator for latency evaluation and that includes a main RISC-V module and the remaining RISC-V cores; and (4) synthesized controllers for energy consumption and area evaluation. The implementations of all simulators, listed below, are accessible in the paper's GitHub repository [10]:

1) **Full-System Simulator:** An in-house C++ simulator that emulates the entire system operation. It incorporates the full-size PIM memory and executes all (offline and online) stages of read mapping. During the offline phase, the simulator partitions the reference genome into crossbars, as described in Section V-B. It then conducts seeding, filtering, and read alignment, as discussed in Sections V-C, V-D, and V-E. The simulator also provides the exact number of linear and affine WF instances and iterations performed by DART-PIM throughout the process. Additionally, it quantifies the total utilized memory capacity and the resulting read-mapping accuracy.

2) **Single-Crossbar Simulator:** An in-house MATLAB [76] simulator that models a single crossbar operation cycle by cycle. This simulator verifies the functionality of algorithms implemented using MAGIC NOR operations within DART-PIM. It provides an exact execution time by computing the number of cycles required for executing linear and affine WF, including pre- and post-processing operations. Additionally, it quantifies the energy consumption by counting the number of write/MAGIC NOR switches and the number of read bits.

3) **RISC-V Simulator:** A GEM5 [15] based simulator, developed to simulate the DART-PIM RISC-V cores (*DP-RISC-V*). A designated module emulates the main RISC-V core, while the other RISC-V cores, used for computing tasks, are modeled by other modules, each with a cache memory. This simulator estimates the execution time of each RISC-V core within the DP-RISC-V, emulating the WF computation distribution between the DP-RISC-V and DP-memory, as well as the communication between them.

4) **PIM/Chip/Bank/Crossbar Controllers:** We synthesized the controllers included in DART-PIM, as depicted in Figure 5, to estimate their area and power consumption. The controllers were designed and implemented in SystemVerilog and synthesized using Synopsys Design Compiler [100], targeting TSMC 28nm CMOS technology.

Our evaluation datasets comprise the full Homo Sapiens (human) reference genome (GRCh38\_latest\_genomic.fna [29]) along with short-read datasets generated by Illumina HiSeq X [50] (HG002.hiseqx.pcr-free.30x.R[1-2].fastq [29]). These datasets comprise 389M reads, each 150 base pairs long.

TABLE III  
SUMMARY OF DART-PIM USED PARAMETERS.

Parameter	Context	Value
Read length ( $rl$ )	Read mapping	150
Minimizer length ( $k$ )	Read mapping	12
Minimizer window length ( $W$ )	Read mapping	30
Linear (affine) error threshold ( $eth$ )	Read mapping	6 (31)
$w_{sub}=w_{ins}=w_{del}=w_{op}=w_{ex}$	Wagner-Fischer	1
Reads FIFO # rows	DART-PIM	160
Linear Buffer # rows	DART-PIM	32
Affine Buffer # rows	DART-PIM	64
Low threshold ( $lowTh$ )	DART-PIM	3
Maximum # allowed read (max reads)	DART-PIM	25k
Low cell resistance ( $R_{on}$ )	RRAM	50k $\Omega$
High cell resistance ( $R_{off}$ )	RRAM	5M $\Omega$

## VII. EXPERIMENTAL RESULTS

The evaluation of DART-PIM is based on extensive simulations performed using the simulators outlined in Section VI and parameters listed in Table III. General parameters (i.e., read-mapping and Wagner-Fischer parameters) were set according to existing literature and remain constant across all simulations. Parameters used specifically in DART-PIM were selected using an exhaustive search to optimize system latency and energy consumption. The linear (affine) buffer size was set to 32 (64) rows, resulting in a Reads FIFO of  $256 - 32 - 64 = 160$  rows (recall the  $256 \times 1024$  crossbar size).

Another important parameter is the low threshold  $lowTh = 3$ . The low threshold balances between DP-memory capacity and RISC-V workload by determining whether affine WF computations are performed by DP-memory (minimizer frequency above  $lowTh$ ) or DP-RISC-V (minimizer frequency below or equal  $lowTh$ ). To avoid highly non-uniform assignment of reads per crossbar, we also bound the number of read handled by any single crossbar to  $maxReads (=12.5k/20k/50k)$ .

This section details the simulated results of DART-PIM's accuracy, execution time, energy consumption, and area, and compares them to minimap2 [71], NVIDIA Parabricks [85], GenASM [19], SeGraM [20] and GeNVoM [62].

### A. DART-PIM Accuracy

To evaluate DART-PIM's accuracy, we compare it to *BWA-MEM* [69] that serves as the ground-truth. Specifically, we compare the locations identified by DART-PIM to those selected by BWA-MEM. Unlike GenASM and SeGraM which use score similarity to approximate accuracy, our accuracy metric is defined as the fraction of DART-PIM mappings that precisely match the corresponding BWA-MEM mapped locations, and as such, it is more meaningful. DART-PIM has an accuracy of 99.7% for  $maxReads$  of 12.5k, and 99.8% for  $maxReads$  of 25k and 50k, while Parabricks and minimap2 each have an accuracy of 99.9% [71], [85]. GenASM and SeGraM both achieve 96.6% accuracy [19], [20], and GenVoM has an accuracy of 91.2% due to its use of heuristics [62].

Figure 8 demonstrates the trade-off between an accelerator's throughput and the achieved mapping accuracy. DART-PIM stands out by optimizing this trade-off, attaining throughput slightly below the state-of-the-art (GeNVoM) while maintaining state-of-the-art accuracy (Parabricks/minimap2). DART-

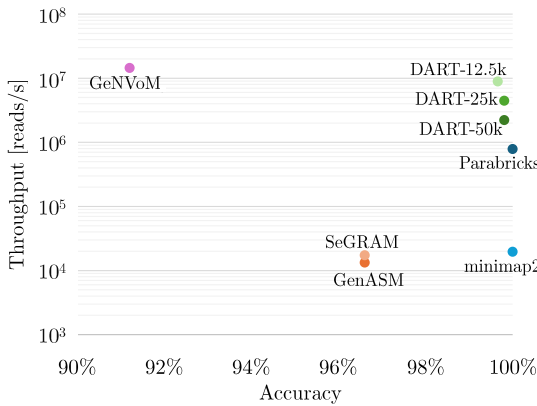


Fig. 8. A comparison of DART-PIM with prior read-mapping accelerators in terms of throughput and accuracy.

TABLE IV

CYCLE AND SWITCH COUNTS FOR EACH MEMORY OPERATION FROM THE SINGLE-CROSSBAR SIMULATOR DURING A SINGLE WF CALCULATION.

		MAGIC NOR	Writes	Reads	Total
Linear	# Cycles	254,585	4035	0	258,620
WF	# Switches	254,384	255,499	0	509,883
Affine	# Cycles	1,288,281	20,418	0	1,308,699
WF	# Switches	1,271,921	1,277,495	0	2,549,416

PIM is positioned similarly when considering the trade-off between accuracy and area/energy efficiencies.

#### B. Single Crossbar Evaluation

The fundamental building block of our performance evaluation is a cycle-accurate simulation of executing WF instances on a single crossbar. The Single-Crossbar simulator counts the overall number of MAGIC NOR switches, number of read bits and write switches, and the number of cycles per operation, encompassing both linear and affine algorithms.

The number of cycles and switches utilized by a single WF instance is outlined in Table IV. Thanks to inter- and intra-crossbar parallelism, multiple WF instances are performed at the same number of cycles. The energy consumption of nucleus operations (write / MAGIC NOR switches), required for calculating the total energy per WF instance, appear in Table V. Given these values, the number of cycles required for the linear (affine) WF is 258,620 (1,308,699), while the overall energy consumed by the linear (affine) WF amounts to 509,883  $\times$  90fJ = 45.9nJ (2,549,416  $\times$  90fJ = 229nJ).

The simulated number of cycles (254,585) fits our theoretical estimates: the total MAGIC NOR cycles for a single linear WF computation is the product of 1950 WF cells ( $2^{eth} + 1 = 13$  cells per row times 150 rows) and 130 cycles

per cell, which amounts to 253,500 cycles. The remaining 1085 cycles are dedicated to the first matrix row/column initializations, and to step ④ in Figure 6.

#### C. DART-PIM Execution Time and Throughput

Figure 9 (left subplot) compares the throughput of DART-PIM, minimap2 [71], NVIDIA Parabricks [85], GenASM [19], SeGram [20], and GeNVoM [62], measured by mapped reads per second. For our selected dataset (389M reads), DART-PIM execution time ranges between 43.8s (maxReads = 12.5k) to 174s (maxReads = 50k). In comparison, minimap2 takes 5.5 hours (19,785s) on a Xeon E5-2683 v4, while Parabricks completes in 8.3 minutes (495s) on DGX A100. GenASM requires 8.1 hours (29,154s), based on the reported 200k reads per 30s. This time is scaled from the original GenASM results with a read length of 250 base pairs to 150 base pairs, according to the throughput ratio of those read lengths. SeGram shows a 1.3 $\times$  throughput improvement over GenASM, resulting in an execution time of 6.23 hours (22,426s). According to GenVoM’s reported throughput, its execution time for our dataset is 39.2s (scaled from reads of 100 to 150 base pairs). When using maxRead = 25k, DART-PIM’s execution time compared to minimap2, Parabricks, GenASM, and SeGram are 227 $\times$ , 5.7 $\times$ , 334 $\times$  and 257 $\times$  better, respectively.

Figure 10a shows the breakdown of DART-PIM’s execution time. The execution time is determined by the maximum of three latency factors: (1) Reading the results from the DP-memory (light green), (2) overall latency of DP-RISC-V computations (purple), and (3) the time required to write the reads to DP-memory and compute within the DP-memory (aggregate of remaining colors). To ensure that DART-PIM is primarily constrained by the computational capabilities of PIM rather than being limited by data transfers or RISC-V processing, the latter should be the most time-consuming.

The DP-memory execution time is determined as

$$T_{DP\text{memory}} = (K_L \cdot N_L + K_A \cdot N_A) \cdot T_{clk}, \quad (6)$$

where  $T_{clk}$  is the clock cycle time (see Table V),  $K_L$  ( $K_A$ ) is the number of linear (affine) iterations (determined by the full-system simulator), and  $N_L$  ( $N_A$ ) is the number of cycles per linear (affine) WF iteration (see Table IV).

The maximal number of reads per crossbar trades off accuracy and execution time: A higher maxReads enhances accuracy, but linearly increases total execution time. As the number of linear/affine WF instances grows sub-linearly with maxReads, the throughput (reads per second) decreases.

We chose to add 128 RISC-V cores (4 per chip) to guarantee that DP-RISC-V do not pose a bottleneck. Assuming all cores are working in parallel, we evaluated their execution time on 0.16% of all affine WF instances to be 19.4s. This underlines the extreme efficiency of DP-memory, as it computes 99.84% of the instances in only four times this latency.

#### D. DART-PIM Energy Efficiency

Figure 9 (middle subplot) compares the energy efficiency [87] of DART-PIM, minimap2, NVIDIA Parabricks,

TABLE V

SUMMARY OF CONSERVATIVELY SCALED MAGIC NOR AND WRITE SWITCHING ENERGY AND CYCLE TIME FROM [103].

Operations	Energy/Time
MAGIC/write conservatively scaled cycle	2ns
MAGIC conservatively scaled energy	90fJ/bit
Write conservatively scaled energy	90fJ/bit

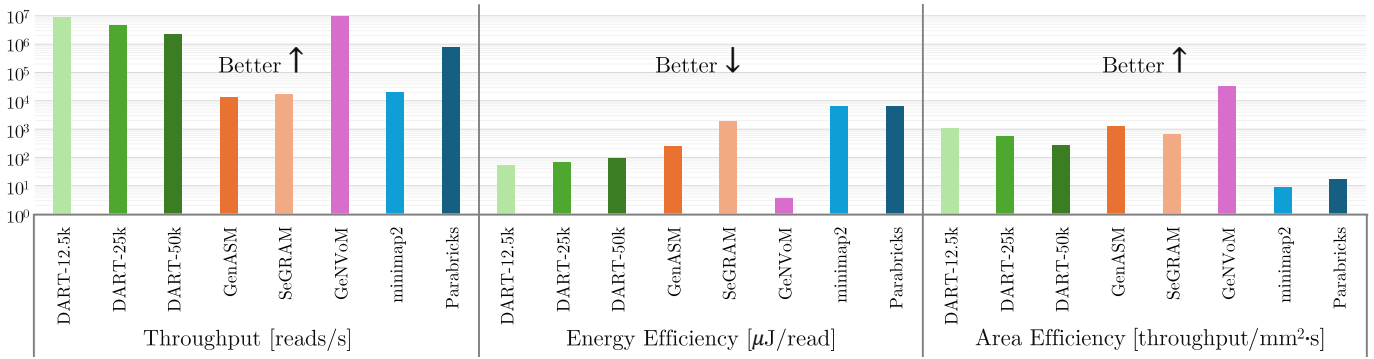


Fig. 9. Comparison of throughput (reads per second), energy efficiency (read per joule), and area efficiency (throughput per squared millimeter) of DART-PIM with different values of maxReads (12.5k, 25K, 50K) and state-of-the-art approaches.

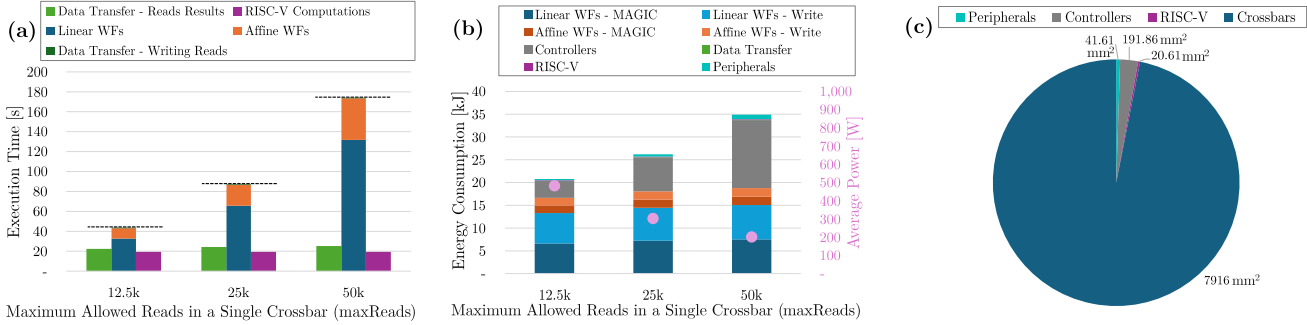


Fig. 10. Performance of DART-PIM for 389 million reads: (a) execution time across various maxReads settings, alongside time of the data transfer and DP-RISC-V computations, (b) energy consumption and average power across different maxReads configurations, and (c) area of crossbars, periphery, controllers, and RISC-V.

GenASM, SeGram, and GeNVoM, measured as the consumed energy per mapped read. For our selected dataset (389M reads), minimap2 and Parabricks both consume 2.4MJ of energy, based on average power consumption of 120W and 4850W, respectively. The energy consumption for GenASM, SeGram, and GeNVoM is 94.2kJ, 543kJ, and 1.4kJ, respectively, based on average power consumption of 3.23W, 24.2W ( $7.5 \times$  GenASM's power), and 35.3W. DART-PIM consumes between 20.8kJ (for  $\text{maxRead} = 12.5\text{k}$ ) and 34.9kJ (for  $\text{maxRead} = 50\text{k}$ ), with average power consumption ranging from 201W to 482W. For  $\text{maxRead} = 25\text{k}$ , DART-PIM achieves a respective improvement of 90.6x over minimap2 and Parabricks, 3.6x over GenASM, and 20.7x over SeGram.

Figure 10b shows a breakdown of DART-PIM's energy consumption to three primary components: DP-memory (controller, peripheral circuits, and crossbars), DP-RISC-V (cores and caches), and the mutual data transfer. Given an energy consumption of  $\mathcal{E}_{MAGIC}$  and  $\mathcal{E}_{WRITE}$  for MAGIC and WRITE operations, respectively, the crossbars energy is determined by

$$\mathcal{E}_{crossbars} = (\mathcal{E}_{MAGIC} \cdot S_L^{MAGIC} + \mathcal{E}_{WRITE} \cdot S_L^{WRITE}) \cdot J_L + (\mathcal{E}_{MAGIC} \cdot S_A^{MAGIC} + \mathcal{E}_{WRITE} \cdot S_A^{WRITE}) \cdot J_A \quad (7)$$

where  $S_L^{MAGIC}$ ,  $S_L^{WRITE}$  and  $J_L$  are the number MAGIC switches, write switches, and instances for linear WF, respectively ( $S_A^{MAGIC}$ ,  $S_A^{WRITE}$  and  $J_A$  are the corresponding parameters for affine WF). Their values appear in Tables V, IV.

The power analysis of the RISC-V cores, detailed in Ta-

TABLE VI  
TIME, ENERGY, AND AREA OF DATA TRANSFER, RISC-V CORES, PERIPHERALS, AND CONTROLLERS (OF A SINGLE UNIT). [CS]/[RVs] INDICATE DATA GENERATED BY THE CONTROLLER/RISC-V SIMULATOR.

Operations	Time	Energy/Power	Area	# Units
Write (DP-RISC-V to DP-memory)	32GB/s [103]	11.7pJ/bit [102]	-	-
Read (DP-memory to DP-RISC-V)	32GB/s [103]	5.64pJ/bit [102]	-	-
RISC-V (single affine SW instance)	88μs [RVs]	40mW [9]	0.11mm <sup>2</sup> [9]	128
RISC-V cache	-	8mW [111]	0.05mm <sup>2</sup> [111]	128
Crossbar controller [Cs]	-	9.43μW	21μm <sup>2</sup>	8M
Bank controller [Cs]	-	0.42mW	939μm <sup>2</sup>	16k
Chip controller [Cs]	-	9.4mW	20,091μm <sup>2</sup>	16
PIM controller [Cs]	-	0.5mW	938μm <sup>2</sup>	1
Decode and Drive Unit [103]	-	129.1μW	277μm <sup>2</sup>	16k
R/W Circuit [103]	-	10pW	0.06μm <sup>2</sup>	8M
Selector Passgates [103]	-	20pW	0.001μm <sup>2</sup>	1024×8M
Driver Passgate [103]	-	20pW	0.001μm <sup>2</sup>	256×8M

ble VI, was conducted using AndesCore AX25 [9]. All RISC-V cores with their caches consume 6.1W of power, as shown in Figure 10b (purple). Based on the controller configuration (Table II) and corresponding controller simulation results (Table VI), the aggregated average power consumption is 86W, yielding the energy consumption in Figure 10b (grey).

The remaining energy consumption corresponds to memory peripherals and data transfers. The peripheral circuits were evaluated by circuit synthesis analysis conducted by RACER [103] (scaled to 28nm) and amounted to 5.7W (see details in Table VI). The data transfer energy comprises the writeout of reads to DP-memory (1.1J) and readout of computation results from the DP-memory (75.4J), as evaluated

by CONCEPT [102]. Figure 10b presents the estimates for memory peripherals (turquoise) and data transfers (green).

Increasing maxReads results in linear growth of execution time and in the controllers' and peripheral devices' energy consumption, while the power consumption remains relatively stable. The energy consumption for DP-memory computations, however, rises only from 16.6kJ at maxReads = 12.5k to 18.8kJ at maxReads = 50k. This increase corresponds to the marginal growth in WF instances computed by DP-memory.

#### E. DART-PIM Area Efficiency

Figure 9 (right subplot) compares the area efficiency [87] of DART-PIM, minimap2, NVIDIA Parabricks, GenASM, SeGraM, and GeNVoM, evaluated as the read-mapping throughput per chip area. DART-PIM's area efficiency spans between  $1086 \frac{\text{reads}}{\text{mm}^2 \cdot \text{s}}$  for maxReads=12.5k and  $273 \frac{\text{reads}}{\text{mm}^2 \cdot \text{s}}$  for maxReads=50K. This positions DART-PIM close to GenASM's and SeGraM's  $1247 \frac{\text{reads}}{\text{mm}^2 \cdot \text{s}}$  and  $623 \frac{\text{reads}}{\text{mm}^2 \cdot \text{s}}$ , respectively, and significantly better than minimap2's and NVIDIA Parabricks' respective  $8.3 \frac{\text{reads}}{\text{mm}^2 \cdot \text{s}}$  and  $16.9 \frac{\text{reads}}{\text{mm}^2 \cdot \text{s}}$ .

We used the reported areas of  $10.7 \text{mm}^2$  for GenASM,  $27.8 \text{mm}^2$  ( $2.6 \times$  GenASM's area) for SeGraM [19], [20],  $298 \text{mm}^2$  for GeNVoM [62], and  $2,362 \text{mm}^2$  for the CPU used by minimap2 [54]. The area of Parabricks was calculated considering eight A100 GPUs, each combined with six HBM stacks of nine 8Gb (eight units and a 8Gb buffer die), each with an area of  $92 \text{mm}^2$  [83], [96]. The total area of A100 GPUs and their HBMs is  $8 \cdot (826 \text{mm}^2 + 6 \cdot 9 \cdot 92 \text{mm}^2) = 46,352 \text{mm}^2$ .

Aggregating its four components, DART-PIM's total area amounts to  $8170 \text{mm}^2$ : (1) crossbar arrays, (2) controllers, (3) memory peripherals, and (4) RISC-V units. Figure 10c shows a breakdown of DART-PIM's area, illustrating that crossbars occupy 96.9% of the area. Since all crossbars perform similar tasks, we were able to substantially simplify the CMOS-based crossbars controllers and save significant chip area.

The areas of all DART-PIM's components are listed in Table VI for CMOS 28nm technology. Specifically, the area of 128 DP-RISC-V cores and caches amounts to  $14.2 \text{mm}^2$  (based on AndesCore AX25 [9]) and  $6.4 \text{mm}^2$ , respectively; the area of the controllers sums up to  $191.9 \text{mm}^2$  (determined by synthesis results); and the peripherals occupy  $53.6 \text{mm}^2$  (based on 15nm synthesis from RACER [103] using the Synopsis Design Compiler, scaled to the target 28nm technology [99]). The remaining area of DART-PIM comprises  $8M$  crossbars, as extracted from the full-system simulator. Based on [45], each crossbar cell has a feature size ( $F$ ) of 30nm, resulting in a memory cell area of  $4F^2 = 3600 \text{nm}^2$ . With a crossbar size of  $256 \times 1024$ , the area per crossbar is  $944 \mu\text{m}^2$  (and  $7916 \text{mm}^2$  for all crossbars). Note that the total memory capacity of DART-PIM is  $8M \times 1024 \times 256$  resulting in  $256 \text{GB}$ . This confirms the practicality of DART-PIM as it aligns with common memory DIMMs, such as the Intel Optane persistent memory [53].

## VIII. RELATED WORK

To the best of our knowledge, DART-PIM represents the first attempt to improve the entire read mapping by eliminating

data movement between the different read mapping stages. By consolidating all stages of read mapping within the same physical memory, PIM effectively eliminates the need for external data transfer. Recent research efforts have primarily focused on accelerating a part of the read mapping process.

Various attempts focused on solely accelerating the indexing and/or filtering stages. Indexing was accelerated both over classical architectures, e.g. GPU [22], FPGA [115] and ASIC (Niubility [108] and EXMA [57]), and using near-memory processing [43] or PIM (FindeR [119], Aligner [118]). Filtering acceleration was also addressed in previous work, including FastHASH [112] for standard CPUs, GRIM Filter [63] for 3D-stacked memory, and embedded dynamic memory based RASSA [58]. Additionally, FPGA-based solutions (e.g., MAGNET [8], GateKeeper [7] and Shouji [6]), alongside PIM and in-storage frameworks, (e.g., FiltPIM [61] and GenStore [74]), leverage parallelism to expedite the filtering process.

Different approaches utilize specialized software or hardware accelerators tailored to the demanding read alignment process. Noteworthy software solutions include Minimap2 [71] and BWA-MEM [69]. On the hardware side, Parasail [24] leverages SIMD-capable CPUs, while GPU-RMAP [2] and GSWABE [73] utilize GPUs. FPGAs were employed by FPGASW [28] and ASAP [12], while ASIC-based accelerators have also been proposed (Darwin [104]). Moreover, GenDP [35] suggests a DP accelerator with programmable compute units. Recently, PIM-based solutions such as [59], RADAR [47], RAPID [36], RAPIDx [114], and BioSEAL [60] offer promising alternatives for more efficient read alignment.

The remainder of relevant prior work includes acceleration of all read-mapping stages. GenAx [31] and its improved version GenCache [79] accelerate each stage individually, but do not consider data transfer in between stages in their performance evaluation. GenPIP [75], on the other hand, integrated read mapping with a preliminary process (called basecalling), and evaluated their acceleration altogether. For a coherent evaluation, we compare DART-PIM only to architectures that accelerate and evaluate the end-to-end read-mapping process: GenASM [19], SeGraM [20], GeNVoM [62].

While GenASM [19] markedly enhances both filtering and read alignment within the logic layer of a 3D-stacked memory, its reliance on data transfers between different stages restricts overall performance improvement. SeGraM [20] improved GenASM by introducing an algorithm/hardware co-design for improving the seeding and read alignment stages, resulting in a throughput enhancement at the cost of energy and area. Finally, GeNVoM [62] employs an associative memristive memory to implement a heuristic search-based procedure, instead of sequence alignment methods (used in this paper). The main problem of this approach is a severe accuracy degradation. In contrast to above solutions, DART-PIM mitigates the data transfer bottleneck and enables very high parallelism by implementing all stages of read mapping in-memory without sacrificing mapping accuracy.

## IX. CONCLUSION

We introduce DART-PIM, a novel framework for accelerating the entire DNA read-mapping process using digital PIM. DART-PIM integrates all stages of read mapping within the same physical crossbars, eliminating the performance and energy costs associated with data transfers. Our evaluation shows that memristive-based DART-PIM achieves significant speedup and improved energy efficiency compared to state-of-the-art existing accelerator and GPU implementations.

The DART-PIM concept and architecture are not limited to RRAM or memristive logic and could be adapted to leverage other PIM techniques, including those based on DRAM, SRAM, and different emerging PIM technologies.

## REFERENCES

- [1] J. Ahn, S. Yoo, O. Mutlu, and K. Choi, “Pim-enabled instructions: A low-overhead, locality-aware processing-in-memory architecture,” *ACM SIGARCH Computer Architecture News*, vol. 43, no. 3S, pp. 336–348, 2015.
- [2] A. M. Aji, L. Zhang, and W.-c. Feng, “Gpu-rmap: accelerating short-read mapping on graphics processors,” in *2010 13th IEEE International Conference on Computational Science and Engineering*. IEEE, 2010, pp. 168–175.
- [3] H. Akinaga and H. Shima, “Resistive random access memory (reram) based on metal oxides,” *Proceedings of the IEEE*, vol. 98, no. 12, pp. 2237–2251, 2010.
- [4] M. Alser, Z. Bingöl, D. S. Cali, J. Kim, S. Ghose, C. Alkan, and O. Mutlu, “Accelerating genome analysis: A primer on an ongoing journey,” *IEEE Micro*, vol. 40, no. 5, pp. 65–75, 2020.
- [5] M. Alser *et al.*, “Accelerating genome analysis: A primer on an ongoing journey,” *IEEE Micro*, 2020.
- [6] M. Alser, H. Hassan, A. Kumar, O. Mutlu, and C. Alkan, “Shouji: a fast and efficient pre-alignment filter for sequence alignment,” *Bioinformatics*, vol. 35, no. 21, pp. 4255–4263, 2019.
- [7] M. Alser, H. Hassan, H. Xin, O. Ergin, O. Mutlu, and C. Alkan, “Gatekeeper: a new hardware architecture for accelerating pre-alignment in dna short read mapping,” *Bioinformatics*, vol. 33, no. 21, pp. 3355–3363, 2017.
- [8] M. Alser, O. Mutlu, and C. Alkan, “Magnet: understanding and improving the accuracy of genome pre-alignment filtering,” *arXiv preprint arXiv:1707.01631*, 2017.
- [9] Andrey Technology, “AndesCore AX25.” [Online]. Available: <https://www.andestech.com/en/products-solutions/andescore-processors/riscv-ax25/>
- [10] Anonymous, “DART-PIM Github Repository.” [Online]. Available: [https://anonymous.4open.science/r/DART\\_PIM\\_Repository-BD54/](https://anonymous.4open.science/r/DART_PIM_Repository-BD54/)
- [11] E. A. Ashley, “Towards precision medicine,” *Nature Reviews Genetics*, vol. 17, no. 9, pp. 507–522, 2016.
- [12] S. S. Banerjee, M. El-Hadedy, J. B. Lim, Z. T. Kalbarczyk, D. Chen, S. S. Lumetta, and R. K. Iyer, “Asap: Accelerated short-read alignment on programmable hardware,” *IEEE Transactions on Computers*, vol. 68, no. 3, pp. 331–346, 2018.
- [13] R. Ben-Hur, N. Wald, N. Talati, and S. Kvatincky, “Simple magic: Synthesis and in-memory Mapping of logic execution for memristor-aided logic,” in *2017 IEEE/ACM International Conference on Computer-Aided Design (ICCAD)*, Nov 2017, pp. 225–232.
- [14] R. Ben-Hur, R. Ronen, A. Haj-Ali, D. Bhattacharjee, A. Eliahu, N. Peled, and S. Kvatincky, “SIMPLER MAGIC: Synthesis and Mapping of In-Memory Logic Executed in a Single Row to Improve Throughput,” *IEEE Transactions on Computer-Aided Design of Integrated Circuits and Systems*, vol. 39, no. 10, pp. 2434–2447, 2020.
- [15] N. Binkert, B. Beckmann, G. Black, S. K. Reinhardt, A. Saidi, A. Basu, J. Hestness, D. R. Hower, T. Krishna, S. Sardashti *et al.*, “The gem5 simulator,” *ACM SIGARCH computer architecture news*, vol. 39, no. 2, pp. 1–7, 2011.
- [16] J. Borghetti, G. S. Snider, P. J. Kuekes, J. J. Yang, D. R. Stewart, and R. S. Williams, “‘Memristive’ Switches Enable ‘Stateful’ Logic Operations via Material Implication,” *Nature*, vol. 464, no. 7290, pp. 873–876, Apr. 2010.
- [17] J. Borghetti, G. S. Snider, P. J. Kuekes, J. J. Yang, D. R. Stewart, and R. S. Williams, “‘Memristive’ switches enable ‘stateful’ logic operations via material implication,” *Nature*, vol. 464, no. 7290, pp. 873–876, 2010.
- [18] C. Børsting and N. Morling, “Next generation sequencing and its applications in forensic genetics,” *Forensic Science International: Genetics*, vol. 18, pp. 78–89, 2015.
- [19] D. S. Cali, G. S. Kalsi, Z. Bingöl, C. Firtina, L. Subramanian, J. S. Kim, R. Ausavarungnirun, M. Alser, J. Gomez-Luna, A. Boroumand *et al.*, “GenASM: A high-performance, low-power approximate string matching acceleration framework for genome sequence analysis,” in *2020 53rd Annual IEEE/ACM International Symposium on Microarchitecture (MICRO)*. IEEE, 2020, pp. 951–966.
- [20] D. S. Cali, K. Kanellopoulos, J. Lindegger, Z. Bingöl, G. S. Kalsi, Z. Zuo, C. Firtina, M. B. Cavlak, J. Kim, N. M. Ghiasi *et al.*, “Segram: A universal hardware accelerator for genomic sequence-to-graph and sequence-to-sequence mapping,” in *Proceedings of the 49th Annual International Symposium on Computer Architecture*, 2022, pp. 638–655.
- [21] S. Canzar and S. L. Salzberg, “Short read mapping: an algorithmic tour,” *Proceedings of the IEEE*, vol. 105, no. 3, pp. 436–458, 2015.
- [22] A. Chacón, S. M. Sola, A. Espinosa, P. Ribeca, and J. C. Moure, “Fm-index on gpu: A cooperative scheme to reduce memory footprint,” in *2014 IEEE International Symposium on Parallel and Distributed Processing with Applications*, 2014, pp. 1–9.
- [23] L. Chin, J. N. Andersen, and P. A. Futreal, “Cancer genomics: from discovery science to personalized medicine,” *Nature medicine*, vol. 17, no. 3, pp. 297–303, 2011.
- [24] J. Daily, “Parasail: Simd c library for global, semi-global, and local pairwise sequence alignments,” *BMC bioinformatics*, vol. 17, pp. 1–11, 2016.
- [25] M. O. Dayhoff, “A model of evolutionary change in proteins,” *Atlas of protein sequence and structure*, vol. 5, pp. 89–99, 1972.
- [26] S. Diab, A. Nassereldine, M. Alser, J. Gómez Luna, O. Mutlu, and I. El Hajj, “A framework for high-throughput sequence alignment using real processing-in-memory systems,” *Bioinformatics*, vol. 39, no. 5, p. btad155, 2023.
- [27] C. Eckert, X. Wang, J. Wang, A. Subramaniyan, R. Iyer, D. Sylvester, D. Blaauw, and R. Das, “Neural cache: Bit-serial in-cache acceleration of deep neural networks,” in *ACM/IEEE International Symposium on Computer Architecture*, 2018, pp. 383–396.
- [28] X. Fei, Z. Dan, L. Lina, M. Xin, and Z. Chunlei, “Fpgasw: accelerating large-scale smith–waterman sequence alignment application with backtracking on fpga linear systolic array,” *Interdisciplinary Sciences: Computational Life Sciences*, vol. 10, pp. 176–188, 2018.
- [29] N. N. C. for Biotechnology Information, “National Library of Medicine,” 2023. [Online]. Available: [https://www.ncbi.nlm.nih.gov/datasets/genome/GCF\\_000001405.40/](https://www.ncbi.nlm.nih.gov/datasets/genome/GCF_000001405.40/)
- [30] D. Fujiki, S. Mahlke, and R. Das, “Duality cache for data parallel acceleration,” in *ACM/IEEE 46th Annual International Symposium on Computer Architecture (ISCA)*, 2019, pp. 1–14.
- [31] D. Fujiki, A. Subramaniyan, T. Zhang, Y. Zeng, R. Das, D. Blaauw, and S. Narayanasamy, “Genax: A genome sequencing accelerator,” in *2018 ACM/IEEE 45th Annual International Symposium on Computer Architecture (ISCA)*. IEEE, 2018, pp. 69–82.
- [32] F. Gao, G. Tzantzioulis, and D. Wentzlaff, “ComputeDRAM: In-memory compute using off-the-shelf DRAMs,” in *IEEE/ACM International Symposium on Microarchitecture (MICRO)*, 2019.
- [33] G. S. Ginsburg and H. F. Willard, “Genomic and personalized medicine: foundations and applications,” *Translational research*, vol. 154, no. 6, pp. 277–287, 2009.
- [34] O. Gotoh, “An improved algorithm for matching biological sequences,” *Journal of molecular biology*, vol. 162, no. 3, pp. 705–708, 1982.
- [35] Y. Gu, A. Subramaniyan, T. Dunn, A. Khadem, K.-Y. Chen, S. Paul, M. Vasimuddin, S. Misra, D. Blaauw, S. Narayanasamy *et al.*, “Gendp: A framework of dynamic programming acceleration for genome sequencing analysis,” in *Proceedings of the 50th Annual International Symposium on Computer Architecture*, 2023, pp. 1–15.
- [36] S. Gupta, M. Imani, B. Khaleghi, V. Kumar, and T. Rosing, “Rapid: A reram processing in-memory architecture for dna sequence alignment,” in *2019 IEEE/ACM International Symposium on Low Power Electronics and Design (ISLPED)*, 2019, pp. 1–6.

[37] S. Gupta, M. Imani, and T. Rosing, "FELIX: Fast and energy-efficient logic in memory," in *IEEE/ACM International Conference on Computer-Aided Design (ICCAD)*, 2018.

[38] S. Gupta, M. Imani, and T. Rosing, "FELIX: Fast and Energy-Efficient Logic in Memory," in *2018 IEEE/ACM International Conference on Computer-Aided Design (ICCAD)*, 2018, pp. 1–7.

[39] N. Hajinazar, G. F. Oliveira, S. Gregorio, J. a. D. Ferreira, N. M. Ghiasi, M. Patel, M. Alser, S. Ghose, J. Gómez-Luna, and O. Mutlu, "SIMDRAM: A framework for bit-serial SIMD processing using DRAM," in *ACM International Conference on Architectural Support for Programming Languages and Operating Systems (ASPLOS)*, 2021.

[40] P. A. Hall and G. R. Dowling, "Approximate string matching," *ACM computing surveys (CSUR)*, vol. 12, no. 4, pp. 381–402, 1980.

[41] M. Hassan, F. M. Awan, A. Naz, E. J. deAndrés Galiana, O. Alvarez, A. Cernea, L. Fernández-Brillet, J. L. Fernández-Martínez, and A. Kloczkowski, "Innovations in genomics and big data analytics for personalized medicine and health care: A review," *International journal of molecular sciences*, vol. 23, no. 9, p. 4645, 2022.

[42] E. C. Hayden, "Technology: The \$1,000 genome," *Nature*, vol. 507, no. 7492, pp. 294–296, 2014.

[43] J. M. Herruzo, I. Fernandez, S. González-Navarro, and O. Plata, "Enabling fast and energy-efficient fm-index exact matching using processing-near-memory," *The Journal of Supercomputing*, vol. 77, no. 9, pp. 10226–10251, 2021.

[44] B. Hoffer, V. Rana, S. Menzel, R. Waser, and S. Kvatinsky, "Experimental Demonstration of Memristor-Aided Logic (MAGIC) Using Valence Change Memory (VCM)," *IEEE transactions on electron devices*, vol. 67, no. 8, pp. 3115 – 3122, 2020. [Online]. Available: <https://user.fz-juelich.de/record/885492>

[45] M.-C. Hsieh, Y.-C. Liao, Y.-W. Chin, C.-H. Lien, T.-S. Chang, Y.-D. Chih, S. Natarajan, M.-J. Tsai, Y.-C. King, and C. J. Lin, "Ultra high density 3d via rram in pure 28nm cmos process," in *2013 IEEE international electron devices meeting (IEDM)*. IEEE, 2013, pp. 10–3.

[46] G. Hu, J. Lee, J. Nowak, J. Z. Sun, J. Harms, A. Annunziata, S. Brown, W. Chen, Y. Kim, G. Lauer *et al.*, "Stt-mram with double magnetic tunnel junctions," in *2015 IEEE International Electron Devices Meeting (IEDM)*. IEEE, 2015, pp. 26–3.

[47] W. Huangfu, S. Li, X. Hu, and Y. Xie, "Radar: A 3d-reram based dna alignment accelerator architecture," in *Proceedings of the 55th Annual Design Automation Conference*, 2018, pp. 1–6.

[48] W. Huangfu, X. Li, S. Li, X. Hu, P. Gu, and Y. Xie, "Medal: Scalable dimm based near data processing accelerator for dna seeding algorithm," in *Proceedings of the 52nd Annual IEEE/ACM International Symposium on Microarchitecture*, 2019, pp. 587–599.

[49] Hybrid Memory Cube Consortium, "Hybrid Memory Cube Specification 2.1," 2015.

[50] Illumina, Inc., "HiSeq X." [Online]. Available: <https://www.illumina.com/systems/sequencing-platforms/hiseq-x/specifications.html>

[51] Illumina, Inc., "NextSeq 1000 and 2000." [Online]. Available: <https://www.illumina.com/systems/sequencing-platforms/nextseq-1000-2000/specifications.html>

[52] Illumina, Inc., "NovaSeq 6000Dx." [Online]. Available: <https://www.illumina.com/systems/ivd-instruments/novaseq-6000dx/specifications.html>

[53] Intel, "Intel Optane Memory." [Online]. Available: <https://www.intel.com/content/www/us/en/products/details/memory-storage/optane-memory.html>

[54] Intel, "Intel Xeon CPU E5-2683 v4 @ 2.10GHz." [Online]. Available: <https://www.intel.com/content/www/us/en/products/sku/91766/intel-xeon-processor-e52683-v4-40m-cache-2-10-ghz/specifications.html>

[55] B. Jacob, D. Wang, and S. Ng, *Memory systems: cache, DRAM, disk*. Morgan Kaufmann, 2010.

[56] JEDEC Solid State Technology Assn., "JESD235C: High Bandwidth Memory (HBM) DRAM," 2020.

[57] L. Jiang and F. Zokaei, "Exma: A genomics accelerator for exact-matching," in *2021 IEEE International Symposium on High-Performance Computer Architecture (HPCA)*, 2021, pp. 399–411.

[58] R. Kaplan, L. Yavits, and R. Ginosar, "Rassa: resistive prealignment accelerator for approximate dna long read mapping," *IEEE Micro*, vol. 39, no. 4, pp. 44–54, 2018.

[59] R. Kaplan, L. Yavits, R. Ginosar, and U. Weiser, "A resistive cam processing-in-storage architecture for dna sequence alignment," *IEEE Micro*, vol. 37, no. 4, pp. 20–28, 2017.

[60] R. Kaplan, L. Yavits, and R. Ginosar, "Bioseal: In-memory biological sequence alignment accelerator for large-scale genomic data," in *Proceedings of the 13th ACM International Systems and Storage Conference*, 2020, pp. 36–48.

[61] M. Khalifa, R. Ben-Hur, R. Ronen, O. Leitersdorf, L. Yavits, and S. Kvatinsky, "Filtpim: In-memory filter for dna sequencing," in *2021 28th IEEE International Conference on Electronics, Circuits, and Systems (ICECS)*. IEEE, 2021, pp. 1–4.

[62] S. K. Khatamifard, Z. Chowdhury, N. Pande, M. Razaviyayn, C. Kim, and U. R. Karpuzcu, "Genvom: Read mapping near non-volatile memory," *IEEE/ACM Transactions on Computational Biology and Bioinformatics*, vol. 19, no. 6, pp. 3482–3496, 2022.

[63] J. S. Kim, D. Senol Cali, H. Xin, D. Lee, S. Ghose, M. Alser, H. Hassan, O. Ergin, C. Alkan, and O. Mutlu, "Grim-filter: Fast seed location filtering in dna read mapping using processing-in-memory technologies," *BMC genomics*, vol. 19, pp. 23–40, 2018.

[64] S. Kvatinsky, D. Belousov, S. Liman, G. Satat, N. Wald, E. G. Friedman, A. Kolodny, and U. C. Weiser, "MAGIC - Memristor-Aided Logic," *IEEE Transactions on Circuits and Systems II: Express Briefs*, vol. 61, no. 11, pp. 895–899, nov 2014.

[65] D. Lee, S. Ghose, G. Pekhimenko, S. Khan, and O. Mutlu, "Simultaneous multi-layer access: Improving 3d-stacked memory bandwidth at low cost," *ACM Transactions on Architecture and Code Optimization (TACO)*, vol. 12, no. 4, pp. 1–29, 2016.

[66] O. Leitersdorf, B. Perach, R. Ronen, and S. Kvatinsky, "Efficient error-correcting-code mechanism for high-throughput memristive processing-in-memory," in *2021 58th ACM/IEEE Design Automation Conference (DAC)*. IEEE, 2021, pp. 199–204.

[67] O. Leitersdorf, R. Ronen, and S. Kvatinsky, "Making memristive processing-in-memory reliable," in *2021 28th IEEE International Conference on Electronics, Circuits, and Systems (ICECS)*. IEEE, 2021, pp. 1–6.

[68] V. I. Levenshtein *et al.*, "Binary codes capable of correcting deletions, insertions, and reversals," in *Soviet physics doklady*, vol. 10, no. 8. Soviet Union, 1966, pp. 707–710.

[69] H. Li, "Aligning sequence reads, clone sequences and assembly contigs with BWA-MEM," *arXiv preprint arXiv:1303.3997*, 2013.

[70] H. Li, "Minimap and miniasm: fast mapping and de novo assembly for noisy long sequences," *Bioinformatics*, vol. 32, no. 14, pp. 2103–2110, 2016.

[71] H. Li, "Minimap2: pairwise alignment for nucleotide sequences," *Bioinformatics*, vol. 34, no. 18, pp. 3094–3100, 2018.

[72] S. Li, D. Niu, K. T. Malladi, H. Zheng, B. Brennan, and Y. Xie, "DRISA: A DRAM-based reconfigurable in-situ accelerator," in *IEEE/ACM International Symposium on Microarchitecture (MICRO)*, 2017.

[73] Y. Liu and B. Schmidt, "Gswabe: faster gpu-accelerated sequence alignment with optimal alignment retrieval for short dna sequences," *Concurrency and Computation: Practice and Experience*, vol. 27, no. 4, pp. 958–972, 2015.

[74] N. Mansouri Ghiasi, J. Park, H. Mustafa, J. Kim, A. Olgun, A. Gollwitzer, D. Senol Cali, C. Firtina, H. Mao, N. Almadhoun Alserr *et al.*, "Genstore: a high-performance in-storage processing system for genome sequence analysis," in *Proceedings of the 27th ACM International Conference on Architectural Support for Programming Languages and Operating Systems*, 2022, pp. 635–654.

[75] H. Mao, M. Alser, M. Sadrosadati, C. Firtina, A. Baranwal, D. S. Cali, A. Manglik, N. A. Alserr, and O. Mutlu, "Genpip: In-memory acceleration of genome analysis via tight integration of basecalling and read mapping," in *2022 55th IEEE/ACM International Symposium on Microarchitecture (MICRO)*, 2022, pp. 710–726.

[76] MathWorks, "Matlab R2021a." [Online]. Available: <https://www.mathworks.com/products/matlab.html>

[77] O. Mutlu, S. Ghose, J. Gómez-Luna, and R. Ausavarungnirun, "Processing data where it makes sense: Enabling in-memory computation," *Microprocessors and Microsystems*, vol. 67, pp. 28–41, 2019.

[78] O. Mutlu, S. Ghose, J. Gómez-Luna, and R. Ausavarungnirun, "Processing data where it makes sense: Enabling in-memory computation," *Microprocessors and Microsystems*, vol. 67, pp. 28–41, 2019. [Online]. Available: <https://www.sciencedirect.com/science/article/pii/S0141933118302291>

[79] A. Nag, C. Ramachandra, R. Balasubramonian, R. Stutsman, E. Giacomin, H. Kambalasubramanyam, and P.-E. Gaillardon, "Gencache: Leveraging in-cache operators for efficient sequence alignment," in

*Proceedings of the 52nd Annual IEEE/ACM International Symposium on Microarchitecture*, 2019, pp. 334–346.

[80] G. Navarro, “A guided tour to approximate string matching,” *ACM computing surveys (CSUR)*, vol. 33, no. 1, pp. 31–88, 2001.

[81] S. B. Needleman and C. D. Wunsch, “A general method applicable to the search for similarities in the amino acid sequence of two proteins,” *Journal of molecular biology*, vol. 48, no. 3, pp. 443–453, 1970.

[82] S. B. Needleman and C. D. Wunsch, “A general method applicable to the search for similarities in the amino acid sequence of two proteins,” *Journal of molecular biology*, vol. 48, no. 3, pp. 443–453, 1970.

[83] NVIDIA, “NVIDIA A100 Tensor Core GPU Architecture.” [Online]. Available: <https://resources.nvidia.com/en-us/genomics-ep/ampere-architecture-white-paper?xs=169656#page=1>

[84] NVIDIA, “NVIDIA DGX A100.” [Online]. Available: <https://images.nvidia.com/aem-dam/Solutions/Data-Center/nvidia-dgx-a100-datasheet.pdf>

[85] NVIDIA, “Parabricks.” [Online]. Available: <https://www.nvidia.com/en-us/clara/parabricks/>

[86] Oxford Nanopore Technologies, “PromethION.” [Online]. Available: <https://nanoporetech.com/>

[87] A. Pedram, S. Richardson, S. Galal, S. Kvatinsky, and M. A. Horowitz, “Dark Memory and Accelerator-Rich System Optimization in the Dark Silicon Era,” *IEEE Design Test*, vol. 34, no. 2, pp. 39–50, Apr. 2017.

[88] N. Peled, R. Ben-Hur, R. Ronen, and S. Kvatinsky, “X-magic: Enhancing pim using input overwriting capabilities,” 10 2020, pp. 64–69.

[89] B. Perach, R. Ronen, B. Kimelfeld, and S. Kvatinsky, “Understanding bulk-bitwise processing in-memory through database analytics,” *IEEE Transactions on Emerging Topics in Computing*, vol. 12, no. 1, pp. 7–22, 2024.

[90] B. Perach, R. Ronen, and S. Kvatinsky, “On consistency for bulk-bitwise processing-in-memory,” in *2023 IEEE International Symposium on High-Performance Computer Architecture (HPCA)*, 2023, pp. 705–717.

[91] J. Reuben, R. Ben-Hur, N. Wald, N. Talati, A. H. Ali, P.-E. Gaillardon, and S. Kvatinsky, “Memristive logic: A framework for evaluation and comparison,” in *2017 27th International Symposium on Power and Timing Modeling, Optimization and Simulation (PATMOS)*, 2017, pp. 1–8.

[92] J. Reuben, R. Ben-Hur, N. Wald, N. Talati, A. H. Ali, P.-E. Gaillardon, and S. Kvatinsky, “Memristive logic: A framework for evaluation and comparison,” in *International Symposium on Power and Timing Modeling, Optimization and Simulation (PATMOS)*, 2017.

[93] M. Roberts, W. Hayes, B. Hunt, S. Mount, and J. Yorke, “Reducing storage requirements for biological sequence comparison,” *Bioinformatics (Oxford, England)*, vol. 20, pp. 3363–9, 01 2005.

[94] M. M. Sabry Aly, T. F. Wu, A. Bartolo, Y. H. Malviya, W. Hwang, G. Hills, I. Markov, M. Wootters, M. M. Shulaker, H.-S. Philip Wong, and S. Mitra, “The n3xt approach to energy-efficient abundant-data computing,” *Proceedings of the IEEE*, vol. 107, no. 1, pp. 19–48, 2019.

[95] V. Seshadri, D. Lee, T. Mullins, H. Hassan, A. Boroumand, J. Kim, M. A. Kozuch, O. Mutlu, P. B. Gibbons, and T. C. Mowry, “Ambit: In-memory Accelerator for Bulk Bitwise Operations Using Commodity DRAM Technology,” in *Proceedings of the 50th Annual IEEE/ACM International Symposium on Microarchitecture*, ser. MICRO-50 ’17, 2017, pp. 273–287.

[96] A. Shilov, “JEDEC Publishes HBM2 Specification as Samsung Begins Mass Production of Chips.” [Online]. Available: <https://www.anandtech.com/show/9969/jedec-publishes-hbm2-specification>

[97] T. F. Smith, M. S. Waterman *et al.*, “Identification of common molecular subsequences,” *Journal of molecular biology*, vol. 147, no. 1, pp. 195–197, 1981.

[98] T. F. Smith, M. S. Waterman *et al.*, “Identification of common molecular subsequences,” *Journal of molecular biology*, vol. 147, no. 1, pp. 195–197, 1981.

[99] A. Stillmaker and B. Baas, “Scaling equations for the accurate prediction of cmos device performance from 180 nm to 7 nm,” *Integration*, vol. 58, pp. 74–81, 2017.

[100] Synopsys, “Design Compiler.” [Online]. Available: <https://www.synopsys.com/implementation-and-signoff/rtl-synthesis-test/dc-ultra.html>

[101] N. Talati, S. Gupta, P. Mane, and S. Kvatinsky, “Logic Design Within Memristive Memories Using Memristor-Aided loGIC (MAGIC),” *IEEE Transactions on Nanotechnology*, vol. 15, no. 4, pp. 635–650, July 2016.

[102] N. Talati, H. Ha, B. Perach, R. Ronen, and S. Kvatinsky, “CONCEPT: A Column Oriented Memory Controller for Efficient Memory and PIM Operations in RRAM,” *IEEE Micro*, vol. 39, pp. 33–43, 2 2019.

[103] M. S. Truong, E. Chen, D. Su, L. Shen, A. Glass, L. R. Carley, J. A. Bain, and S. Ghose, “RACER: Bit-pipelined processing using resistive memory,” in *MICRO-54: 54th Annual IEEE/ACM International Symposium on Microarchitecture*, 2021, pp. 100–116.

[104] Y. Turakhia, G. Bejerano, and W. J. Dally, “Darwin: A genomics co-processor provides up to 15,000 x acceleration on long read assembly,” *ACM SIGPLAN Notices*, vol. 53, no. 2, pp. 199–213, 2018.

[105] E. Ukkonen, “Algorithms for approximate string matching,” *Information and control*, vol. 64, no. 1-3, pp. 100–118, 1985.

[106] E. Ukkonen, “Algorithms for approximate string matching,” *Information and Control*, vol. 64, no. 1, pp. 100–118, 1985, international Conference on Foundations of Computation Theory. [Online]. Available: <https://www.sciencedirect.com/science/article/pii/S0019995885800462>

[107] R. A. Wagner and M. J. Fischer, “The string-to-string correction problem,” *Journal of the ACM (JACM)*, vol. 21, no. 1, pp. 168–173, 1974.

[108] Y. Wang, X. Li, D. Zang, G. Tan, and N. Sun, “Accelerating fm-index search for genomic data processing,” in *Proceedings of the 47th International Conference on Parallel Processing*, 2018, pp. 1–12.

[109] Z. Wei, T. Takagi, Y. Kanazawa, Y. Katoh, T. Ninomiya, K. Kawai, S. Muraoka, S. Mitani, K. Katayama, S. Fujii *et al.*, “Demonstration of high-density reram ensuring 10-year retention at 85 °C based on a newly developed reliability model,” in *2011 international electron devices meeting*. IEEE, 2011, pp. 31–4.

[110] H.-S. P. Wong, S. Raoux, S. Kim, J. Liang, J. P. Reifenberg, B. Rajendran, M. Asheghi, and K. E. Goodson, “Phase change memory,” *Proceedings of the IEEE*, vol. 98, no. 12, pp. 2201–2227, 2010.

[111] S.-Y. Wu, J. Liaw, C. Lin, M. Chiang, C. Yang, J. Cheng, M. Tsai, M. Liu, P. Wu, and C. Chang, “A highly manufacturable 28nm cmos low power platform technology with fully functional 64mb sram using dual/tripe gate oxide process,” in *2009 Symposium on VLSI Technology*. IEEE, 2009, pp. 210–211.

[112] H. Xin, D. Lee, F. Hormozdiari, S. Yedkar, O. Mutlu, and C. Alkan, “Accelerating read mapping with fasthash,” in *BMC genomics*, vol. 14. Springer, 2013, pp. 1–13.

[113] C. Xu, D. Niu, N. Muralimanohar, R. Balasubramonian, T. Zhang, S. Yu, and Y. Xie, “Overcoming the challenges of crossbar resistive memory architectures,” in *2015 IEEE 21st International Symposium on High Performance Computer Architecture (HPCA)*, Feb 2015, pp. 476–488.

[114] W. Xu, S. Gupta, N. Moshiri, and T. S. Rosing, “Rapidx: High-performance reram processing in-memory accelerator for sequence alignment,” *IEEE Transactions on Computer-Aided Design of Integrated Circuits and Systems*, vol. 42, no. 10, pp. 3275–3288, 2023.

[115] C.-H. Yang, Y.-C. Wu, Y.-L. Chen, C.-H. Lee, J.-H. Hung, and C.-H. Yang, “An fm-index based high-throughput memory-efficient fpga accelerator for paired-end short-read mapping,” *IEEE Transactions on Biomedical Circuits and Systems*, vol. 17, no. 6, pp. 1331–1341, 2023.

[116] Y. Yang, B. Xie, and J. Yan, “Application of next-generation sequencing technology in forensic science,” *Genomics, proteomics & bioinformatics*, vol. 12, no. 5, pp. 190–197, 2014.

[117] L. Zhang, S. Cosemans, D. J. Wouters, G. Groeseneken, M. Jureczak, and B. Govoreanu, “Selector design considerations and requirements for 1 sir rram crossbar array,” in *2014 IEEE 6th International Memory Workshop (IMW)*. IEEE, 2014, pp. 1–4.

[118] F. Zokaei, H. R. Zarandi, and L. Jiang, “Aligner: A process-in-memory architecture for short read alignment in rerams,” *IEEE Computer Architecture Letters*, vol. 17, no. 2, pp. 237–240, 2018.

[119] F. Zokaei, M. Zhang, and L. Jiang, “Finder: Accelerating fm-index-based exact pattern matching in genomic sequences through reram technology,” in *2019 28th International Conference on Parallel Architectures and Compilation Techniques (PACT)*. IEEE, 2019, pp. 284–295.